

# InGaAs focal plane array for transient astronomy in the NIR

Marcus Birch<sup>Ⓢ</sup>,<sup>a,\*</sup> Jamie Soon,<sup>a</sup> Tony Travouillon<sup>Ⓢ</sup>,<sup>a</sup> Trevor Mendel,<sup>a</sup>  
Brian Taylor<sup>Ⓢ</sup>,<sup>a</sup> and Blaise C. Kuo Tiong<sup>b,c</sup>

<sup>a</sup>Australian National University, Research School of Astronomy and Astrophysics,  
Weston Creek, Australia

<sup>b</sup>Macquarie University, Department of Physics and Astronomy, New South Wales, Australia

<sup>c</sup>Macquarie University, MQ Photonics Research Centre, Department of Physics and Astronomy,  
New South Wales, Australia

**Abstract.** An indium-gallium-arsenide (InGaAs) detector is tested for use on the new Dynamic REd All-sky Monitoring Survey (DREAMS) 0.5-m telescope. DREAMS is novel for its use of InGaAs as a higher-noise and lower-cost alternative to mercury-cadmium-telluride. The Princeton Infrared Technologies 1280SCICAM, which has one of the smallest pitches and largest focal planes of any commercially available InGaAs detector, is extensively characterized to determine the viability of InGaAs detectors for astronomy. We find the 1280SCICAM to have the one of the lowest dark currents ( $67e^-/s$ ) of any commercially available InGaAs focal plane array, and also confirm no fringing or non-linearity is present. Given its low noise, we conclude that DREAMS will be sufficiently background limited with InGaAs, and by extension, InGaAs is well-suited for application on low-angular-resolution NIR instruments. © 2022 Society of Photo-Optical Instrumentation Engineers (SPIE) [DOI: [10.1117/1.JATIS.8.1.016001](https://doi.org/10.1117/1.JATIS.8.1.016001)]

**Keywords:** indium gallium arsenide; detector; infrared; noise; dark current.

Paper 21053 received May 4, 2021; accepted for publication Jan. 4, 2022; published online Jan. 27, 2022.

## 1 Introduction

Dynamic RED All-sky Monitoring Survey (DREAMS) is a 0.5-m telescope to be commissioned in 2022 at Siding Spring Observatory as the first telescope capable of rapidly scanning the southern sky for near-IR (NIR) transients for every 6 to 7 nights.<sup>1</sup> DREAMS will be a partner to the northern hemisphere Palomar Gattini-IR survey telescope commissioned in 2019, also aiming to detect reddened transient events and to cooperate with visible transient surveys such as Pan-STARRS and the upcoming Vera Rubin Observatory.<sup>2-4</sup> The key examples of science DREAMS will engage in are searching for electromagnetic counterparts to gravitational waves and discovering supernovae obscured by dust. The primary motivation for a high-cadence, transient survey in the NIR is therefore detecting reddened transients that are brighter in the NIR.<sup>5-8</sup> DREAMS will survey in the J band (1.17 to 1.33  $\mu\text{m}$ ) and a shortened H band, H' (1.49 to 1.67  $\mu\text{m}$ ). Indium gallium arsenide (InGaAs) has an intrinsic cutoff at 1.67  $\mu\text{m}$ , i.e., approximately half of the standard H band (1.49 to 1.78  $\mu\text{m}$ ) is covered.

DREAMS is novel for its use of commercial-off-the-shelf (COTS) InGaAs detectors, marking one of the first major applications of InGaAs for astronomical imaging. DREAMS will use six COTS Princeton Infrared Technologies (PIRT) 1280SCICAMs, a  $1280 \times 1024$  InGaAs focal plane array (FPA), for a total 3.5 square degrees field-of-view (FOV) at 2.5 arcseconds/pixel.

The NIR sky is  $\sim 250$  times brighter than the visible, therefore, a smaller pixel scale is needed to reduce the amount of sky sampled per pixel.<sup>9</sup> Achieving a smaller pixel scale while maintaining the large FOV required for mapping the sky every week subsequently requires a large pixel count. The very high cost of low-noise NIR detectors has therefore limited the construction

---

\*Address all correspondence to Marcus Birch, [marcus.birch@anu.edu.au](mailto:marcus.birch@anu.edu.au)

of the large cameras required of survey telescopes.<sup>1</sup> InGaAs facilitates these large cameras due to its significantly lower price. The viability of InGaAs for this application is reliant on it meeting DREAMS survey requirements, i.e., DREAMS must stay background limited for exposure times of  $\sim 10$  s at the 2.5 arcseconds/pixel pixel scale. This exposure time was selected as a trade-off between AB magnitude depths of  $m_I = 17.4$  and  $m_{H'} = 17.2$  at zenith, and a 6 to 7 day cadence. Target-of-opportunity searches, e.g., for gravitational wave alerts, will be more sensitive than the survey. Dithering for accurate background subtraction, site cloudiness, and target of opportunity searches, are among the numerous other factors involved in this cadence estimation.

A relatively high-noise InGaAs FPA for high background (low angular resolution) astronomical imaging was demonstrated by Sullivan et al.,<sup>10</sup> though our array is an improvement on the  $640 \times 512$  FLIR AP640C FPA tested in that work. The 1280SCICAM has the smallest non-export controlled pixel size for InGaAs at  $12 \mu\text{m}$  per pixel, and is the first InGaAs array to be available at a large format ( $1280 \times 1024$  pixels). We also consider a full COTS solution with control board and thermoelectric cooling down to  $-60^\circ\text{C}$  included with the 1280SCICAM as a significant advantage over competing InGaAs products. A thermoelectric cooler simplifies engineering requirements compared with the cryogenics required for mercury-cadmium-telluride (HgCdTe) to reach  $\sim 70$  K.

We characterize one 1280SCICAM in the lab, testing for parameters, such as read noise, dark current, non-linearity, and fringing. Persistence was tested, but yielded negligible results and was limited by the sensitivity of the detector itself. Given the bright NIR sky background, persistence is also minor consideration for DREAMS. Testing typically involved exposing the 1280SCICAM to an integrating sphere, which is illuminated by a 1550-nm super-luminescent diode (SLD), shown in Fig. 1. However, dark current and read noise testing did not require illuminating the detector; instead, it required covering the array with a black cap and, in the case of dark testing, cooling down the environment in a thermal chamber. All non-differential measurements used subtraction of bias frames that were taken in conditions outlined in Section 3. The detector is controlled and data are received using an EDT Visionlink F4 frame-grabber and the Camera Link communication protocol.<sup>11,12</sup> Software for interfacing with the detector was written in Python.<sup>13–16</sup> Readout with the 1280SCICAM is limited to correlated double sampling, i.e., methods such as Fowler sampling and sample up-the-ramp are not possible. All testing used fan cooling due to a lack of appropriate glycol chiller; however, we intend to operate all six 1280SCICAMs with liquid cooling on DREAMS. While fan cooling cannot typically reach the 1280SCICAMs minimum temperature of  $-60^\circ\text{C}$ , this was possible when the detector was cooled in a thermal chamber.

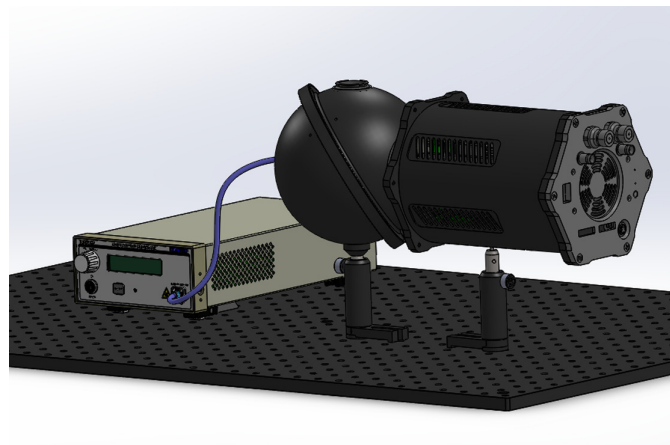


**Fig. 1** Experimental configuration for characterization of the PIRT 1280SCICAM. SLD is shown illuminating integration sphere through multi-mode fiber. 1280SCICAM is abutting adjacent port of integration sphere, with internal baffle stopping direct (non-reflected) light.

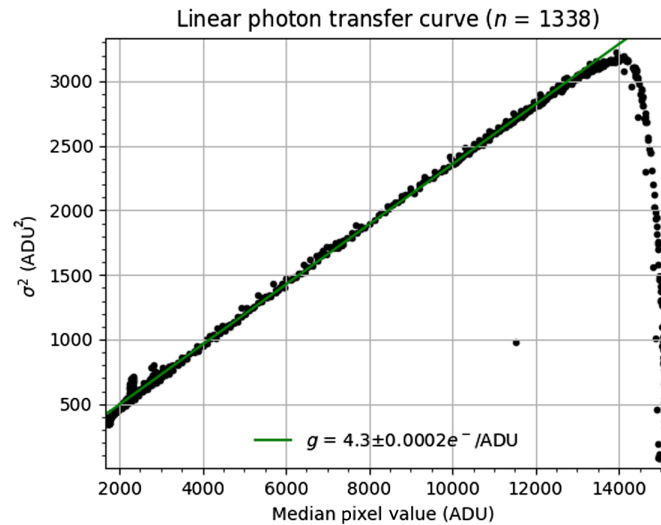


**Fig. 2** Linear PTC from 1338 difference images and 2676 raw frames. Slope used to determine gain is fitted over linear portion of PTC. Non-linearity and full well can be seen for high pixel values.

## 2 Gain

Gain ( $g$ ) is estimated with the slope of a linear photon transfer curve (PTC), i.e., intensity against variance.<sup>17,18</sup> A linear PTC method is chosen over the standard log–log form because it provides more robust fitting for gain. Determining  $g$  from the PTC requires measuring the intensity-variance slope for the most linear portion of the detector well, and specifically where it is photon shot noise-limited.

We construct a PTC from a detector integration time (DIT) ramp under constant illumination, i.e., a series of exposures with increasing DIT to sample the range of possible pixel values.<sup>18,19</sup> Holding the SLD at a low power (<1 mW) for dim illumination ensures the DIT ramp samples the detector range with high resolution. At each DIT, a pair of images are taken and the variance is calculated from the difference image while the intensity is recorded from a single image. Difference images are employed throughout testing to measure only the random noise by removing fixed pattern noise. A linear portion of the detectors' well is sampled, starting at ~2000 ADUs, to fit the gain slope where shot noise dominates and read noise is minimal.

PTC results are shown in Fig. 2, yielding  $4.3 e^-/\text{ADU}$  for our 1280SCICAM. Figure 2 shows the typical behavior of a PTC at full well, i.e., variance falls off as pixels saturate and are no longer dominated by shot noise. Although the gain cannot readily be tuned to custom values with the 1280SCICAM, optimization testing of bias voltages may be done in the commissioning process for DREAMS.

## 3 Read Noise

For the purpose of this paper, we define readout noise (RN) as the total RN, i.e., all signal-independent noise contributions that occurs every readout. The 1280SCICAM has a fixed readout method with minimal scope for calibrating internal electronics, so we cannot discern voltage conversion and amplification noise.

We estimate RN by exposing the detector for the minimum allowable DIT on the 1280SCICAM,  $33 \mu\text{s}$ . Images are taken in pairs to create difference images and subtract fixed pattern noise, which is done 1000 times (2000 raw frames). The mean standard deviation of these 1000 difference images is then said to be the RN (with a  $\sqrt{2}$  division to account for the central limit theorem). RN is tested with/without conditioned power, i.e., a voltage stabilizer between the detector and mains power, particularly as voltage fluctuations are a common problem with non-scientific COTS products. Results of RN testing are given in Table 1.

**Table 1** Read noise as a function of FPA temperature for conditioned and unconditioned power. Gain of  $4.3e^-/\text{ADU}$ .

FPA temperature ( $^{\circ}\text{C}$ )	Conditioned power ( $e^-$ )	Unconditioned power ( $e^-$ )
20	$83.8 \pm 0.2$	$83.9 \pm 0.3$
0	$83.5 \pm 0.2$	$83.5 \pm 0.2$
-20	$82.4 \pm 0.2$	$82.4 \pm 0.2$
-40	$79.9 \pm 0.3$	$79.9 \pm 0.3$

We find that RN is highly stable, and conditioned power has no effect. RN as a function of temperature is within the bounds of dark current ( $I_{\text{dark}}$ ) temperature dependence for a  $33 \mu\text{s}$  DIT, as found in Sec. 6. A second-order extrapolation of measurements in Table 1 down to  $-60^{\circ}\text{C}$  yields  $\approx 77.4 e^-$  ( $-60^{\circ}\text{C}$  could not be reached in the laboratory at the time of testing but will be the operational temperature of DREAMS).

Bias frames used throughout this characterization were constructed from an average of the many minimum exposure time frames taken for RN testing, and for each FPA temperature as a temperature dependence was identified. Bias values ranged from  $5100 e^-$  to  $7300 e^-$  for the FPA at  $20^{\circ}\text{C}$  and  $-60^{\circ}\text{C}$ , respectively.

#### 4 Full Well

Full well of the 1280SCICAM is measured by taking 70 oversaturated (DIT = 20 s is orders of magnitude above required saturation time for given illumination) images and producing a median-stacked final image. Figure 3 shows this median-stacked image on the right and its corresponding pixel distribution histogram on the left. Variance of saturation values is low, also shown by Fig. 2, as it is typically governed by minor fabrication or voltage non-uniformities. The two horizontal bands of high full well in Fig. 3(b) could be caused by dopant concentration or alloy thickness, as it was independent of illumination method.<sup>20</sup>

A  $\mu - 3\sigma$  value is used to define a full well value of  $56.885 ke^-$  ( $g = 4.3 e^-/\text{ADU}$ ),<sup>19</sup> i.e., a lower bound where  $\sim 1\%$  of pixels become saturated.<sup>19</sup> Full well measurement in combination with RN yields a dynamic range of 735:1.

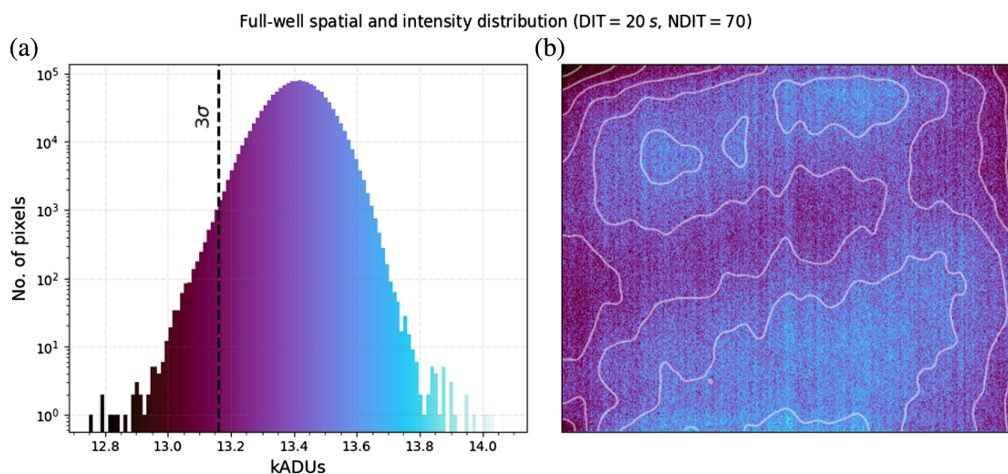


**Fig. 3** Full well analysis from median stack of 50 oversaturated frames with DIT = 20 s. (a) Pixel distribution histogram with black dotted line marking point  $3\sigma$  under mean. (b) Spatial map with contours showing banded distribution of high full well.

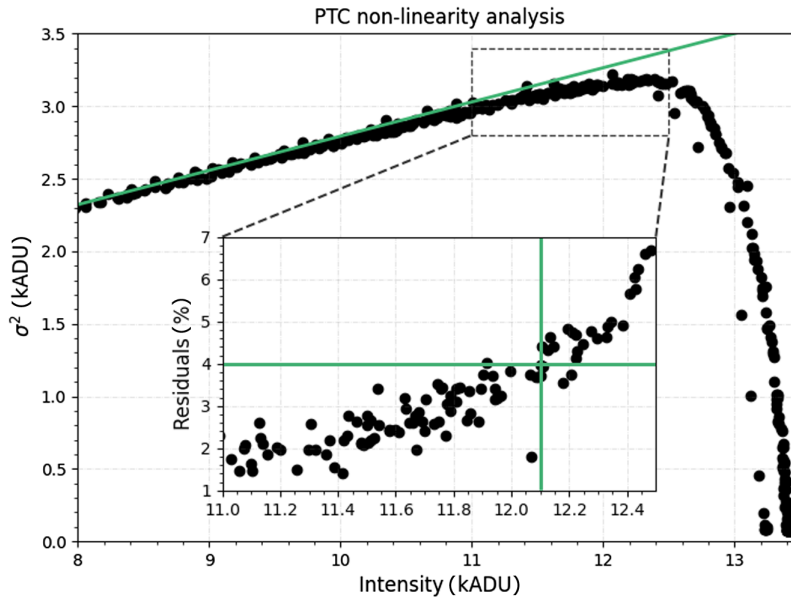


**Fig. 4** Linear photon-transfer curve near transition to full well, with residuals shown in inset. Point of 4% non-linearity shown with green lines in residuals inset.

## 5 Non-Linearity

Non-linearity analysis is done with a high resolution ( $n = 1250$ ) PTC near full well to identify a point of divergence from a linear fit we deem intractable. We take the conventional 4% divergence from linearity as our threshold, i.e., in survey operation we will define the 4% non-linearity as a functional saturation point.<sup>21</sup> This follows the same method as Fig. 2, but focusing only on the turnover point before full well. Figure 4 shows the resultant PTC in linear-space with fit residuals to quantify non-linearity.

A 4% non-linearity threshold is identified at  $\sim 12.1$  kADUs or  $52 ke^-$ , therefore, any science operation will stay below this range. The  $52 ke^-$  threshold corresponds to linearity over 91% of dynamic range. Further testing of these arrays will measure non-linearity at different FPA temperatures as there is no literature on this for InGaAs, and Biesiadzinski et al.<sup>22</sup> shows a temperature dependence exists for HgCdTe.

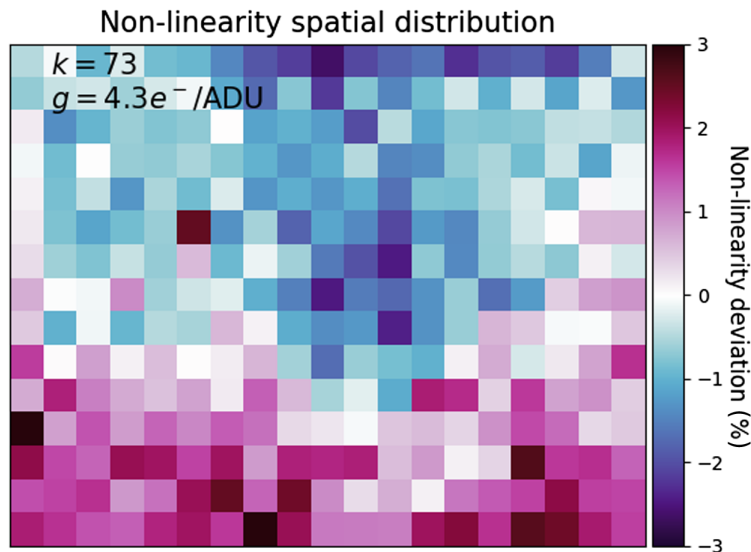


**Fig. 5** Non-linearity map constructed from 73 non-linear frames. Color shows deviation from the mean degree of FPA non-linearity.

## 5.1 Spatial Non-Linearity

We produce non-linearity spatial maps following the procedure of reciprocity failure (count-rate non-linearity) maps from Biesiadzinski et al.<sup>22</sup> We analyze linearity residuals from images near full well on a spatial map by binning images into  $64 \times 64$  domains and effectively calculating PTCs per domain as in Fig. 4. The positive lower portion of the array is found to be more linear than the negative top of the array. The cause of this spatial non-linearity is unclear, it may be caused by the readout integrated circuit (ROIC) and a non-uniform distribution of pixel gains, or a wafer thickness defect. More FPAs would be required to draw a robust conclusion on this finding.

## 6 Dark Current

$I_{\text{dark}}$  competes with sky background to determine if DREAMS will be background-limited, assuming the survey exposures of  $\sim 10$  s exceed the RN-limited regime (see Sec. 10), therefore we deem  $I_{\text{dark}}$  the most important characterization parameter.

For  $I_{\text{dark}}$  testing, a black cap was placed over the FPA to minimize incident photons and the entire device was cooled in a thermal-cycling chamber to reduce thermal emission from the cap. Dark current was measured with 60 frames equally spaced in DIT on a ramp up to 40 s and plotted as a function of DIT.  $I_{\text{dark}}$  is then estimated from the slope of a linear fit, i.e., the count rate. This process was performed over the parameter space of FPA and cap temperature. We specify cap temperature here because the cap reached equilibrium well above chamber temperature (thermocouples were placed around the 1280SCICAM to determine these temperature difference.).

$I_{\text{dark}}$  as a function of FPA temperature at constant cap temperature is shown in Table 2. Table 3 shows  $I_{\text{dark}}$  for cap temperatures at a constant  $-60^\circ\text{C}$  FPA temperature. We see from Table 3 that thermal emission is a small contribution when the detector is sufficiently cooled. Table 3 also shows the temperature difference between the chamber and cap.

This detector appears to have a very low  $I_{\text{dark}}$  ( $0.0075 - 0.008$  nA/cm<sup>2</sup> current density at  $-60^\circ\text{C}$ ), one of the lowest  $I_{\text{dark}}$  for TEC-cooled InGaAs FPAs presented in publicly available literature.<sup>10,23–26</sup> Similar  $I_{\text{dark}}$  results can be found in Yuan et al.,<sup>27</sup> showing  $0.3$  nA/cm<sup>2</sup> at  $-20^\circ\text{C}$  compared with  $0.24$  nA/cm<sup>2</sup> for the 1280SCICAM at  $-20^\circ\text{C}$ .

$I_{\text{dark}}$  measured here is beneath specifications, i.e., the manufacturer quote  $I_{\text{dark}} = 300 - 500$  e<sup>-</sup>/s at  $-60^\circ\text{C}$ . We believe the discrepancy with PIRT is due to their

**Table 2**  $I_{\text{dark}}$  for FPA temperatures ( $-10.6^\circ\text{C}$  cap).

FPA ( $^\circ\text{C}$ )	$I_{\text{dark}}$ (e <sup>-</sup> /s)
-60	68
-40	559
-20	2937

**Table 3**  $I_{\text{dark}}$  for different cap and thermal chamber temperatures ( $-60^\circ\text{C}$  FPA).

Cap [ $^\circ\text{C}$ ]	Chamber ( $^\circ\text{C}$ )	$I_{\text{dark}}$ (e <sup>-</sup> /s)
-5	-10	73
-11	-20	68
-13	-25	67

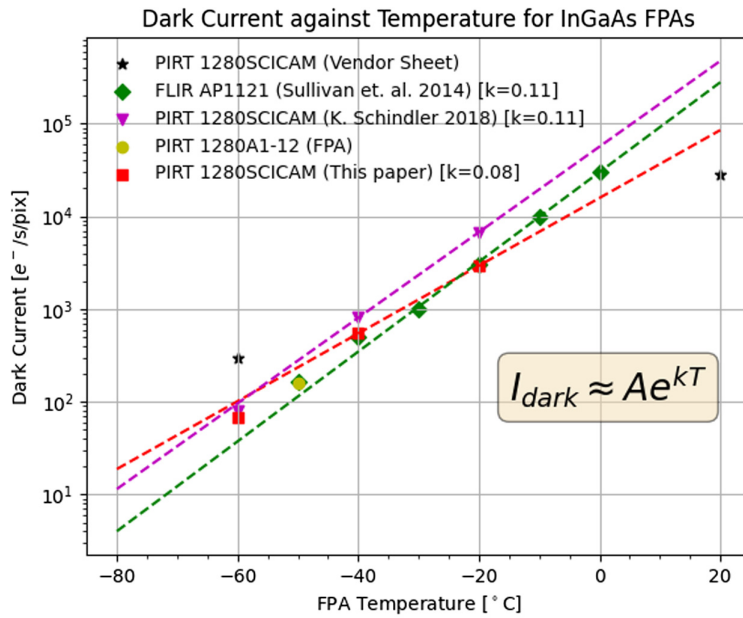


**Fig. 6** Dark current against FPA temperature for a number of data sets. This characterization is shown in red.

characterization with a room temperature cap. Tiong et al.<sup>28</sup> presents characterization of two different 1280SCICAMs with  $I_{\text{dark}} = 284 - 330 \text{ e}^-/\text{s}$  when measured at room temperature.  $I_{\text{dark}}$  as a function of FPA temperature is plotted in Fig. 6, confirming our results are more aligned with expectations than specifications indicate. 1280SCICAM results from K. Schindler (Deutsches SOFIA Institut, personal correspondence), and a FLIR AP1121 (similar 15  $\mu\text{m}$  pitch InGaAs FPA) characterized by Simcoe et al.<sup>23</sup> shown in Fig. 6 were conducted in a cooled environment.

## 7 ROIC Glow

Frames used for  $I_{\text{dark}}$  testing showed a glow from the right side of the array, and a small bright spot. These features are highlighted on a contrast-enhanced image in Fig. 7. Glow from the right

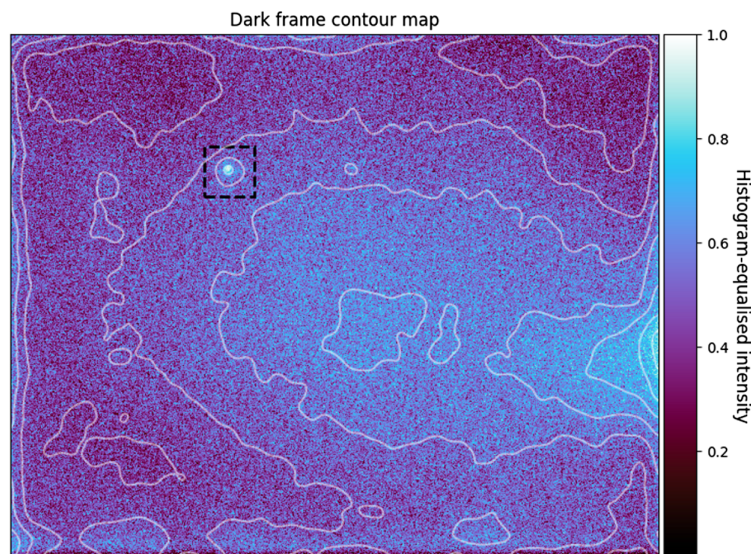


**Fig. 7** Dark frame with contour plot overlaid. Bright spot highlighted with dashed black box. Intensity units are arbitrary and imposed by histogram equalization.

**Table 4** Bad pixel statistics.

Pixel type	$n_{\text{pix}}$
Dead	95
Hot	1558–1777
Unstable (base mode)	547–799
Total	2187–2476 (0.17 ± 0.01% of FPA)

side of the array is believed to be from the ROIC, as amplifiers and multiplexing electronics sit along this side of the array, particularly as other 1280SCICAMs show a similar glow.<sup>28</sup> Further work and coordination with the manufacturer will aim to determine if this contributes to the measured  $I_{\text{dark}}$  floor and look at mitigation methods if this is the case.

## 8 Bad Pixels

We determine the population of bad pixels on the array, i.e., dead pixels, hot pixels, or a class we identify as “unstable pixels” (See Table 4). These unstable pixels occasionally behave as hot pixels, flashing on and off at undetermined intervals. We find significantly more unstable pixels if the camera is run in the Camera Link full mode protocol, and a correlation between horizontal neighboring pixels.<sup>11</sup>

Full mode is a high bitrate (95 fps at full frame) form of the Camera Link protocol, requiring two cables, as opposed to the standard single cable base mode (24 fps at full frame).<sup>11</sup> 65% of unstable pixels were found to be in horizontal pairings when run in full mode, compared to 0.6% in base mode. A likely explanation for this row-wise systematic error is one of the two additional Channel-Link chipsets used in full mode being faulty.<sup>11</sup> Regardless, full mode is not required for DREAMS and was avoided for all other testing. Further spatial correlations were ruled out by running a neighbor classification algorithm on the total bad pixel mask.

## 9 Fringing

We attempted to measure fringing, i.e. internal reflections within the pixels. However, as the 1280SCICAM is substrate-removed with a  $\text{Si}_3\text{N}_4$  layer between pixels and the ROIC (filling the space around Indium bumps), we did not expect fringing to occur.<sup>29</sup> Nonetheless, we deem it an important test given the sparse literature on InGaAs characterization.

Testing required narrowband exposures near the intrinsic InGaAs 1.67  $\mu\text{m}$  cutoff, to compare with narrowband exposures far from this cutoff. This was done with a  $1650 \pm 10$  nm filter in the H region, a  $1250 \pm 10$  nm filter in the J region, and a broadband halogen lamp. Figure 8 shows these images and their difference. Non-uniformity is evident on the lower portion of the H image,

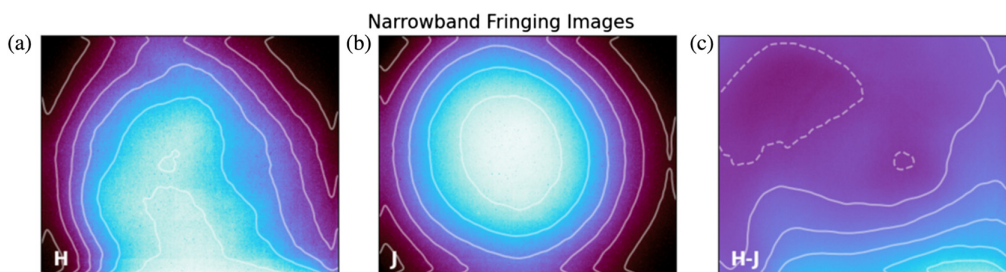


**Fig. 8** Halogen source imaged through  $1650 \pm 10$  nm H and  $1250 \pm 10$  nm J narrowband filters. (a) H image showing filter-induced aberration at bottom of array. (b) J image. (c) Difference map between J and H.

however we find it co-rotates with filter optics and is therefore not a property of the FPA. The upper left region of the difference image also co-rotates with filter optics. A histogram bimodality test in the manner of Wong et al.<sup>30</sup> similarly yielded a null result.

## 10 Detector Performance

Table 5 compares results of this characterization with three alternate InGaAs FPAs, and HgCdTe for reference. The FLIR AP1121 and LYNRED-SOFRADIR SNAKE are viable alternatives but not yet available at a large format. The Raptor Photonics Ninox 1280 is the only other InGaAs COTS FPA at a large format, and with a smaller 10  $\mu\text{m}$  pitch, but does not support liquid cooling and is under export-control.

As introduced in Sec. 1, DIT  $\approx 10$  s is selected as the standard exposure DREAMS will use to cover the sky every 6 to 7 days due to trade offs between cadence and magnitude depth. We are able to operate at this depth due to the pixel scale afforded using six low cost 1280SCICAMs. Faster and shallower surveys do not require as many detectors, e.g., Palomar Gattini-IR has a cadence of two days and depth of 15.8 magnitudes achieved with one 2048  $\times$  2048 HgCdTe detector and a 25 square degree FOV.<sup>4</sup>

We then justify using the low cost 1280SCICAM over HgCdTe if it meets the DREAMS survey requirements, i.e., background limited with DIT  $\approx 10$  s for sky brightness at a 2.5 arcseconds/pixel. Sky brightness is estimated from Sánchez et al.,<sup>34</sup> which measures brightness at zenith in the J and H bands at Calar Alto Observatory, Spain. We deem upper limits (variations of  $\pm 0.5$  magnitudes are readily observed at all sites over a range of timescales.) of Calar Alto as similar to Siding Springs Observatory, where DREAMS will operate, given other extensive surveys of NIR sky brightness have been conducted at significantly drier and higher altitude sites. For the DREAMS 2.5 arcsecond/pixel pixel scale,  $m_{\text{sky,H}} = 13.8$  AB mag/arcsecond and  $m_{\text{sky,J}} = 14.9$  AB mag/arcsecond approximately correspond to 3000  $e^-/\text{s}$  and 1600  $e^-/\text{s}$  respectively. We also make the simplification that spectral flux density is constant across H, such that sky brightness is the same in H' (as limited by 1.67  $\mu\text{m}$  InGaAs cutoff). This assumption is justified because the abundance of OH<sup>-</sup> lines, which dominate sky brightness at this wavelength, are roughly constant across H.<sup>35</sup>

**Table 5** Characterization results for 1280SCICAM in comparison with similar InGaAs FPAs and HgCdTe FPA.

	Our testing	InGaAs			HgCdTe
		Ninox 1280 <sup>a</sup>	FLIR AP1121	SNAKE	HxRG
Read noise ( $e^-$ )	75	<190/ < 50	43	30	8–20 <sup>b</sup>
Dark current ( $e^-/\text{s}$ )	67	<2000	113	290–600	0.01
Full well ( $ke^-$ )	55.16	450/10	80	43	80–150
Dynamic range ( $i:1$ )	735	2368/200	1860	1433	12500–7500
Linearity (%)	91	N/A	N/A	NA	75–90
Inoperable pixels (%)	0.17	<0.5	N/A	<0.5	<0.5 <sup>c</sup>
Size	1024 $\times$ 1280	1024 $\times$ 1280	640 $\times$ 512	640 $\times$ 512	$\leq 4096 \times 4096$

**Notes:** Ninox 1280 characterization results are from Raptor Photonics manufacturer specifications.<sup>32</sup> Characterization results for the FLIR AP1121 are from Simcoe et al. (2019).<sup>23</sup> HxRG characterization results mostly from Blank et al.<sup>31</sup> for an H2RG. LYNRED/SOFRADIR SNAKE characterization from manufacturer and Feautrier et al.<sup>33</sup> Entries listed as N/A mean that no characterization of this parameter has been recorded.

<sup>a</sup>Low gain/high gain specifications shown.

<sup>b</sup>8 – 20  $e^-$  is for CDS readout, can reach 3  $e^-$  for Fowler sampling.<sup>31</sup>

<sup>c</sup>In practice this is typically <0.1%.

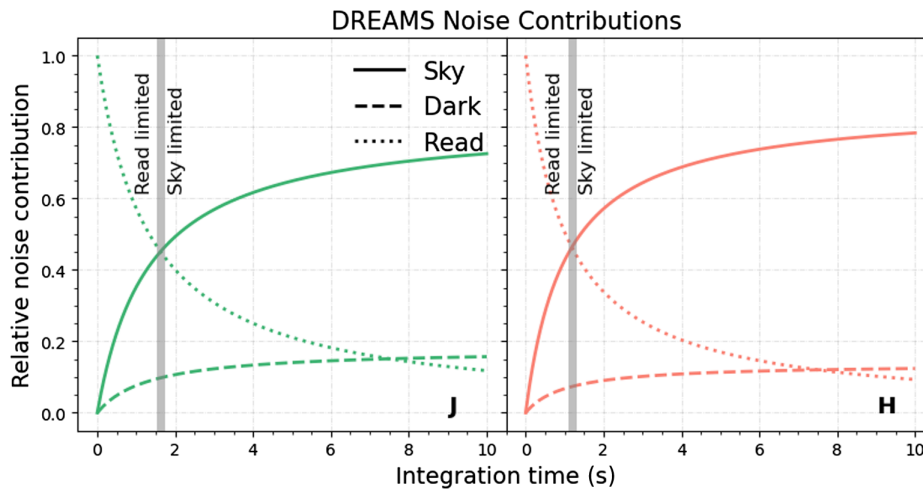


**Fig. 9** Relative noise contributions for DREAMS, including read noise, dark current noise, and sky background noise. Relative noise is defined as the ratio between particular noise sources and the total noise, for a given integration time.

Figure 9 shows relative noise contributions as a function of DIT, given the characterized noise properties of the 1280SCICAM, and sky brightness in J and H' at the DREAMS pixel scale. We see from Fig. 9 that DREAMS will be sufficiently background-limited for DIT  $\approx 10$  s, i.e., sky brightness contributes 80% of noise. An equivalent analysis for HgCdTe at the same plate-scale leads to sky brightness contributing  $>95\%$  of noise. The discrepancy between 80% and 95% is small enough to largely ignore dark noise and justify using InGaAs over HgCdTe for this application. By extension, this also shows that new large format and low  $I_{\text{dark}}$  InGaAs detectors, such as the 1280SCICAM, can viably be used as a low-cost alternative to HgCdTe for large pixel scales.

## 11 Conclusion

We have characterized the first InGaAs array to be commercially available at a large format and found it to have low  $I_{\text{dark}}$  ( $67 e^-/s$ ), and is free of problems common to NIR detectors such as excessive non-linearity. Minor spatial non-uniformities were detected in full well, non-linearity, and amplifier glow, which were spatially uncorrelated (Figs. 3, 5, and 7 respectively). We aim to conduct further testing of the 1280SCICAM with the other five detectors that will be used on DREAMS, particularly to constrain our current results and confirm  $I_{\text{dark}}$  is consistently as low as we present here.

These favorable qualities in addition to its all-in-one COTS implementation and significantly lower cost than HgCdTe lead us to conclude that InGaAs is uniquely positioned for low angular resolution NIR instruments. DREAMS is utilizing the low-cost InGaAs to make a large NIR camera, as one of the first major applications of InGaAs for astronomical imaging, and the first NIR transient survey of the southern sky.

## Acknowledgments

This work was supported by the Australian National University Major Equipment Grant.

## References

1. J. Soon et al., “Opening the dynamic infrared sky,” *Proc. SPIE* **10700**, 107004D (2018).
2. N. Kaiser et al., “The Pan-STARRS wide-field optical/NIR imaging survey,” *Proc. SPIE* **7733**, 77330E (2010).

3. Ž. Ivezić et al., “LSST: from science drivers to reference design and anticipated data products,” *Astrophys. J.* **873**(2), 111 (2019).
4. K. De et al., “Palomar Gattini-IR: survey overview, data processing system, on-sky performance and first results,” *Publ. Astron. Soc. Pac.* **132**(1008), 025001 (2020).
5. L. Tartaglia et al., “The early detection and follow-up of the highly obscured type II supernova 2016ija/DLT16am,” *Astrophys. J.* **853**(1), 62 (2018).
6. M. M. Kasliwal et al., “Spirits: uncovering unusual infrared transients with Spitzer,” *Astrophys. J.* **839**(2), 88 (2017).
7. A. Goobar et al., “The rise of SN 2014j in the nearby galaxy M82,” *Astrophys. J. Lett.* **784**(1), L12 (2014).
8. P. Cowperthwaite et al., “The electromagnetic counterpart of the binary neutron star merger LIGO/Virgo GW170817. II. UV, optical, and near-infrared light curves and comparison to kilonova models,” *Astrophys. J. Lett.* **848**(2), L17 (2017).
9. A. M. Moore and M. M. Kasliwal, “Unveiling the dynamic infrared sky,” *Nat. Astron.* **3**(1), 109–109 (2019).
10. P. W. Sullivan, B. Croll, and R. A. Simcoe, “Near-infrared InGaAs detectors for background-limited imaging and photometry,” *Proc. SPIE* **9154**, 91541F (2014).
11. Automated Imaging Association, “Specifications of the camera link interface standard for digital cameras and frame grabbers, version 1.1” (2000).
12. “EDT VisionLink F4,” 2021, <https://edt.com/product/visionlink-f4/>.
13. C. R. Harris et al., “Array programming with NumPy,” *Nature* **585**(7825), 357–362 (2020).
14. P. Virtanen et al., “SciPy 1.0: fundamental algorithms for scientific computing in Python,” *Nat. Methods* **17**(3), 261–272 (2020).
15. J. D. Hunter, “Matplotlib: A 2D graphics environment,” *Comput. Sci. Eng.* **9**(3), 90–95 (2007).
16. S. Van der Walt et al., “Scikit-image: image processing in Python,” *PeerJ* **2**, e453 (2014).
17. J. Janesick, K. Klaasen, and T. Elliott, “CCD charge collection efficiency and the photon transfer technique,” *Proc. SPIE* **0570**, 7–19 (1985).
18. G. R. Hopkinson, T. M. Goodman, and S. R. Prince, *A Guide To The Use And Calibration Of Detector Array Equipment*, Vol. **142**, SPIE Press, Bellingham, Washington, DC (2004).
19. I. S. McLean, *Electronic Imaging in Astronomy: Detectors and Instrumentation*, Praxis Publishing Ltd., Chichester, UK (2008).
20. M. D. McCluskey and E. E. Haller, *Dopants and Defects in Semiconductors*, CRC Press, Boca Raton, Florida (2018).
21. A. Plazas et al., “Nonlinearity and pixel shifting effects in HXRG infrared detectors,” *J. Instrum.* **12**(4), C04009 (2017).
22. T. Biesiadzinski et al., “Reciprocity failure in HgCdTe detectors: measurements and mitigation,” *Publ. Astron. Soc. Pac.* **123**(906), 958 (2011).
23. R. A. Simcoe et al., “Background-limited imaging in the near infrared with warm InGaAs sensors: applications for time-domain astronomy,” *Astron. J.* **157**(2), 46 (2019).
24. B. M. Onat et al., “Ultra-low dark current InGaAs technology for focal plane arrays for low-light level visible-shortwave infrared imaging,” *Proc. SPIE* **6542**, 65420L (2007).
25. P. Yuan et al., “Low-dark current 1024 × 1280 InGaAs PIN arrays,” *Proc. SPIE* **9070**, 907007 (2014).
26. X. Li et al., “The development of InGaAs short wavelength infrared focal plane arrays with high performance,” *Infrared Phys. Technol.* **80**, 112–119 (2017).
27. H. Yuan et al., “Low dark current small pixel large format InGaAs 2D photodetector array development at Teledyne Judson Technologies,” *Proc. SPIE* **8353**, 835309 (2012).
28. B. C. K. Tiong et al., “Suitability of COTS InGaAs detectors for ground based exoplanet detections around nearby M-dwarfs,” *Proc. SPIE* **11454**, 114542G (2020).
29. G. Finger et al., “Performance evaluation, readout modes, and calibration techniques of HgCdTe Hawaii-2RG mosaic arrays,” *Proc. SPIE* **7021**, 70210P (2008).
30. M. H. Wong, “Fringing in the WFC3/UVIS detector,” in *2010 Space Telescope Science Institute Calibration Workshop - Hubble after SM4*, Preparing JWST (2010).

31. R. Blank et al., “H2RG focal plane array and camera performance update,” *Proc. SPIE* **8453**, 845310 (2012).
32. G. Martin, “High performance SWIR imaging cameras,” Raptor Photonics White Papers, Raptor Photonics Ltd., Larnie, United Kingdom (2015).
33. P. Feautrier et al., “The C-RED fast infrared camera family for wavefront sensing.”
34. S. F. Sánchez et al., “The night sky at the calar alto observatory ii: the sky at the near-infrared,” *Publ. Astron. Soc. Pac.* **120**(873), 1244 (2008).
35. P. Rousselot et al., “Night-sky spectral atlas of oh emission lines in the near-infrared,” *Astron. Astrophys.* **354**, 1134–1150 (2000).

Biographies of the authors are not available.